The Media Calibration System for Cassini Radio Science: Part II

G. M. Resch,[1] J. E. Clark,[2] S. J. Keihm,[3] G. E. Lanyi,[1] C. J. Naudet,[1] A. L. Riley,[3]
H. W. Rosenberger,[3] and A. B. Tanner[3]

A new media calibration system is currently being implemented at DSS 25 that is intended to calibrate the delay of radio signals due to the neutral atmosphere, both the static dry and static and fluctuating wet components of this delay. In particular, the system will calibrate the fluctuations in path delay due to atmospheric water vapor that we believe will dominate the error budget for several radio science and radio astronomy experiments. The first user of this system will be the Gravitational Wave Experiment (GWE) with the Cassini spacecraft. The system consists of a water vapor radiometer (WVR) of a new design (i.e., the A-series), a microwave temperature profiler (MTP), and a package of instruments that sense surface meteorology. In order to demonstrate the performance of the media calibration system, we have installed two of them, one near DSS 13 and one near DSS 15. We operated these two radio antennas as an interferometer and compared the estimates of path delay provided by the media calibration system to the delay fluctuations seen by the interferometer. In this article, we describe the instrumentation, observing strategy, data analysis procedures, and weather conditions for 29 interferometer experiments that started on August 17, 1999, and ended May 18, 2000. Our goal is to demonstrate that the new media calibration system can meet or exceed an Allan standard deviation of 3×10^{-15} on time scales of 1,000 to 10,000 s, as required by the Cassini GWE.

I. Introduction

We expect line-of sight delay fluctuations due to water vapor to be a major error source for the Gravitational Wave Experiment (GWE) with the Cassini spacecraft that is scheduled to start in December 2001 and repeat in 2002 and 2003 during the spacecraft cruise to Saturn. This experiment has been described by Armstrong et al. [1] and Tinto and Armstrong [2]. In order to calibrate fluctuations in the line-of-sight path delay, two redundant media calibration systems have been designed, constructed, and recently installed at DSS 25, the primary DSN station for Cassini radio science experiments.

---

[1] Tracking Systems and Applications Section.

[2] Allied Signal, Honeywell Technical Services, Inc., Pasadena, California.

[3] Microwave and Lidar Technology Section.

The research described in this publication was carried out by the Jet Propulsion Laboratory, California Institute of Technology, under a contract with the National Aeronautics and Space Administration.

To test this new media calibration system, we have used it in a series of 29 experiments with a radio interferometer and compared the two very different techniques for sensing path-delay fluctuations. In this article, we describe the instrumentation that was used, the conditions under which the experiments were performed, and the data analysis procedures. Preliminary results have been reported by Resch et al. [3] and in Part I of this series of articles [4].

The experiments described here were modeled after the ones described in [5] and [6] using water vapor radiometers (WVRs) of an earlier design. The basic concept of the experiment is illustrated schematically in Fig. 1. The radio interferometer is sensitive to any difference in the path of the signal to the two elements comprising the interferometer. The interferometric observable is the phase-delay difference between the signals arriving at each antenna. We model and subtract geometric effects so that, in principle, the residual phase is dominated by effects we cannot model, e.g., fluctuations due to water vapor.

The media calibration system, deployed within 50 m of each antenna, measures the line-of-sight (LOS) delay due to water vapor in the direction of the compact radio source observed with the interferometer. The estimates of LOS delay from each are differenced and then compared with the residual interferometer delay. If we have modeled all known error sources correctly in the interferometer data, if the media calibration system is working as it is designed to do, and if water vapor fluctuations really do dominate the residual delay variations, then we would expect a high degree of correlation between the residual interferometer phase and the differenced media calibration system data streams. This is, in fact, what is observed most of the time. We can then use the differenced WVR data to calibrate and reduce the interferometer residuals. The measure of our success is whether we can demonstrate that this calibration holds to an Allan standard deviation (ASD) of 3×10^{-15} over time scales of 1,000 to 10,000 s, the requirement for the Cassini GWE.

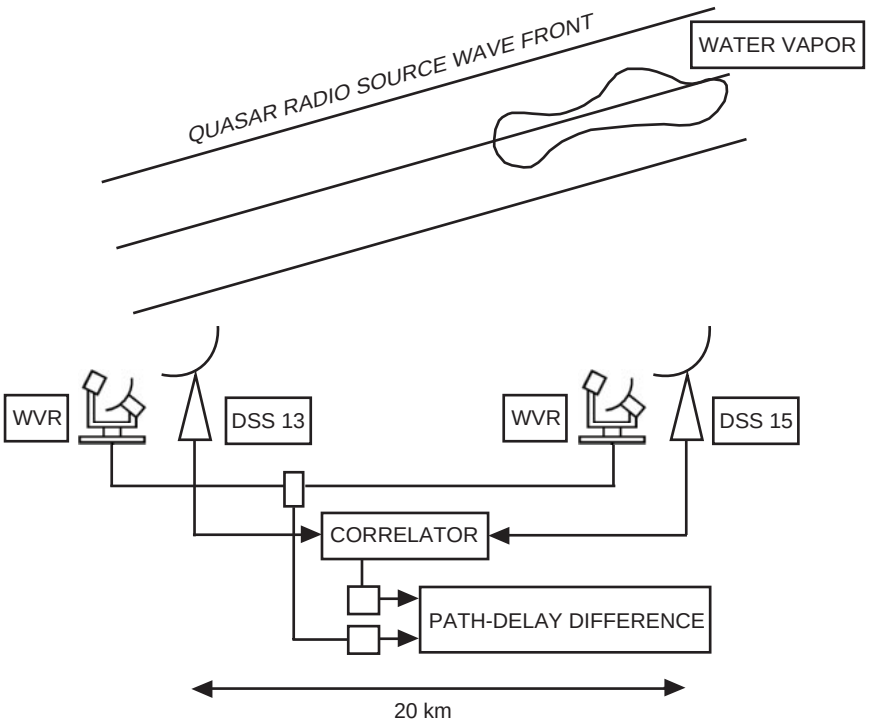

Fig. 1. A schematic illustration of the comparison experiments between a radio interferometer and the new media calibration system constructed to support radio science experiments with the Cassini spacecraft.

II. The Radio Interferometer

We used DSS 13 and DSS 15 for all of our experiments, with the two antennas configured as a connected-element interferometer operating with an approximately 21-km baseline [7]. For a few experiments, we added DSS 65 (Spain) or DSS 45 (Australia). All of these 34-m antennas were equipped to receive at the 2.3 GHz (S-band) and 8.45 GHz (X-band) frequencies, and each has a sensitivity of approximately 0.25 K/Jy. The total system temperatures at DSS 15, DSS 45, and DSS 65 were typically 35 K at S-band and 38 K at X-band, while DSS 13 had 38 K and 40 K at S- and X-band, respectively. Each antenna was also equipped with a Mark IV data acquisition terminal (DAT). A radio source of 1-Jy flux density provides a signal-to-noise ratio (SNR) of approximately 15 for our basic integration time of 2 s in the 2-MHz bandwidth of a DAT channel. For most of our experiments, particularly on the short baseline, we observed very strong radio sources so that we were rarely SNR limited at time scales longer than a few seconds.

A fiber-optic cable was used to distribute the primary frequency reference (a hydrogen maser) to the frequency distribution systems at each antenna. The fiber-optic cable was buried approximately 1.5 m below the desert floor and was temperature stable on time scales of days [8]. However, cables between the control room at DSS 13 and the pedestal area under the antenna were partially exposed and therefore subject to larger temperature variations. The distribution of a single frequency reference to the two radio telescopes made this a connected-element interferometer (CEI), with better long-term phase stability than a very long baseline interferometer (VLBI).

Another fiber-optic cable was used to send a subset of digital data (14 of 28 channels, each of 4 Mb/s data rate) from the Mark IV DAT at DSS 15 to the control room at DSS 13, where the data streams from each antenna were cross-correlated using a slightly modified version of the Block II correlator [9], known as the Real Time Block II or RTB2. This provided a real-time confirmation of interferometer performance and supplied the primary data for our subsequent analysis. In the experiments involving DSS 45 or DSS 65, we recorded data on the tapes of the Mark IV DAT for later cross-correlation at the Block II correlator in Pasadena.

III. The Media Calibration System

The media calibration system (MCS) consists of an advanced water vapor radiometer (AWVR) of a new design (i.e., the A-series), a microwave temperature profiler (MTP), and a group of instruments that sense surface meteorology (SurfMet). To minimize down time during Cassini radio science experiments, the system is redundant, consisting of identical pairs of each instrument. During the interferometry experiments, one complete instrument suite was located within 50 m of the base of each of the 34-m antennas comprising the CEI.

The AWVR is a room-temperature Dicke radiometer with additive noise injection for gain calibration. The instrument measures atmospheric emissions at three frequencies in the vicinity of the 22-GHz resonance line of atmospheric water vapor. The 22.2-GHz channel is the most sensitive to total water-vapor content. The 23.8-GHz channel has 20 percent less sensitivity to the total water vapor, but is insensitive to variations in the vapor height distribution. The 31.4-GHz channel is used primarily to correct for the emission contributions of suspended cloud liquid (when present). Absolute calibration to $\sim$0.3 K accuracy is achieved by performing a series of tipping curves. The 1-second thermal noise is $\sim$0.07 K in each of the channels. Extensive thermal control of the radiometer electronics housing produces long-term stability of $\sim$0.01 K (equivalent to $\sim$0.03 mm of path delay) on time scales of 10,000 s. The antenna is an offset-fed parabolic reflector that minimizes contaminating radiation from scattering and side lobes and has a beam width of 1 deg (full width at half maximum). The azimuth and elevation steering mechanisms are designed to allow complete sky coverage with 0.1-deg pointing accuracy and 0.01-deg pointing knowledge in elevation. A more detailed description of the AWVR is provided by Tanner [10].

During the CEI experiments, each AWVR was controlled separately, and the pointing schedules were coordinated such that each instrument observed the same direction in the sky as the nearby 34-m antenna to within 0.1 deg. Brightness temperatures were recorded each 0.4 s together with the azimuth and elevation pointing information. These data comprised the primary observable set for subsequent retrievals of the wet path-delay time series at either end of the interferometer baseline.

The two microwave temperature profilers (MTPs) were designed and built by Radiometrics Corporation of Boulder, Colorado. These instruments measure sky brightness temperatures at selected frequencies in the 51- to 59-GHz wing of the molecular oxygen spectral band centered at 60 GHz. Because the atmosphere is optically thick at these frequencies and oxygen is well mixed in the lower troposphere, the brightness temperature is a weighted measure of the physical temperature of the air. The variation of brightness temperature with elevation angle can be inverted to yield physical temperature versus height through the lower 5 to 7 km of the troposphere.

A brightness temperature calibration accuracy of 0.5 K is achieved with the MTP by using an internal ambient reference and an external liquid nitrogen (∼78 K) target. The liquid nitrogen target is used to calibrate a noise diode (performed every 3 months), which is then used to monitor gain drifts between calibrations. The antenna steering mechanism permits all-sky pointing with elevation accuracy of ∼0.1 deg. The effective beam width (full width at half power) varies between 2.3 and 2.5 deg over the 51- to 59-GHz channel settings. More detailed description can be found in the reference manual provided by Radiometrics Corporation [11].

During the CEI experiments, the MTPs were operated in a repeating 13-minute elevation scanning mode, measuring sky brightness temperatures at three selected frequencies at elevations of 30, 45, 90, 135, and 150 deg in a single azimuth slice. The 13-minute sampling interval is adequate for monitoring tropospheric temperatures that typically vary by less than 0.1 K on 10-minute time scales. A previous study by Keihm[4] showed that a three-frequency operating mode (53.00, 54.40, and 57.97 GHz), with the above elevation sampling, is near optimum for temperature profiling in the lower 5 km, where almost all of the water vapor resides.

The group of instruments that measure surface meteorological conditions consists of temperature, pressure, relative humidity, wind speed, and wind direction sensors. All are commercially available products. The MET3 weather station, made by Paroscientific of Redmond, Washington, measures ambient temperature, pressure, and relative humidity. The sensor specifications provided by Paroscientific [12] are 0.5 deg C accuracy and 0.01 deg C precision for temperature, 0.1 mb accuracy and 0.001 mb resolution for pressure, and 2 percent accuracy for relative humidity. The MET3 units are returned to the manufacturer annually for recalibration.

The SurfMet instrumentation also includes a sonic anemometer, manufactured by Climatronics of Bohemia, New York, which provides measurements of surface wind speed and direction. The sensor specifications provided by Climatronics [13] are 1.1 m/h accuracy and 0.22 m/h resolution for wind speed, and 5 deg accuracy and 1 deg resolution for wind speeds in excess of 5 m/h.

For the CEI experiments, 1-minute averages of the temperature, pressure, and relative humidity SurfMet data were used in the estimates of path delay. The wind data were evaluated in a qualitative manner in regard to correlations with path-delay fluctuation levels and overall performance of the media calibration system.

---

[4] S. J. Keihm, *Report to Radiometrics on Optimum Channel Selection for a 50-60 GHz MTP*, JPL internal document, Jet Propulsion Laboratory, Pasadena, California, 1993.

IV. The Experiments

Table 1 summarizes the 29 experiments completed in late 1999 and early 2000. We list the scheduled start date, the actual start time of data acquisition (in Universal time, UT), stop time, and duration, and also illustrate schematically the distribution of the observations during day/night hours. Our primary scheduling request was for night hours in order to mimic the conditions under which the GWE would be performed. The initial observing strategy was to observe a variety of strong sources for approximately 26 minutes each. In this way, we were able to track phase fluctuations over a reasonably long period and verify that we could do this at a variety of azimuth and elevation angles. For the experiments in year 2000, we concentrated on longer scans (up to 5 hours) in order to investigate the long-term calibration capability of the media calibration system. Total observing time for these experiments amounted to 174.5 hours.

It was not always possible to obtain antenna time during the night, as can be seen in Table 1. Also, we "piggybacked" on several other VLBI experiments between DSS 15 and DSS 65 or between DSS 15 and DSS 45. For these piggyback experiments, we observed a much longer list of radio sources with greater geometric distribution. The time on each source was approximately 2.5 minutes, and the data were used to determine the DSS 13–DSS 15 baseline.

Table 2 lists the surface meteorology data taken from the weather station at DSS 13 during each experiment and the zenith path delay (ZPD) as estimated by the MCS at each antenna. The data were filtered to cover only the actual times of observation. The average value of each parameter is listed along with the standard deviation about the average. The ZPD variability is a useful indicator of turbulence.

Table 3 lists the surface meteorology data from the MCS located at DSS 15 and from the weather instruments at Signal Processing Center (SPC) 10. The separation of these instrument packages is on the order of 300 m. Note the SurfMet instruments were installed as they became available but after our experiments started in late 1999. We were not able to install wind speed and direction sensors at the DSS-15 location, so those columns are blank in Table 3.

We rely primarily on data from the SurfMet package of sensors in our data analysis, but when it was not available we use the data from the weather stations at DSS 13 and SPC 10. Both were within a few hundred meters of the SurfMet instruments, which were closer to the antennas at DSS 13 and DSS 15. Figures 2 and 3 show scatter plots of the overlapping surface meteorological data from the DSS-13 weather station (the x-axis) and the SurfMet package (the y-axis). In Fig. 2, we plot the pressure, temperature, and relative humidity. Each figure also provides the analytical expression for the regression line of the data. In general, the correlation is very good and, except for the pressure, the offsets are reasonable. In Fig. 3, we plot the wind direction and wind speed. Here, a 180-deg convention between the sensors is apparent. The DSS-13 sensor reports the direction the wind is coming from while the SurfMet package reports the direction the wind is heading. Note that the prevailing wind at DSS 13 is from the west by southwest. Our MCS is located on a line to the southeast of the 34-m antenna, which means that surface winds blow almost perpendicularly to the line between the MCS and the antenna it is calibrating. This geometry, together with the prevailing winds, tends to suppresses short-term correlation between the MCS and CEI data.

In Fig. 4, we show the scatter plots between the SurfMet data (x-axis) and the weather station data at SPC 10. The regression line formula is provided for each plot. Again, the correlation is good and the bias terms small. We conclude that we can use either the SurfMet data or the weather-station data at Goldstone (corrected by the regression lines) and maintain consistency in our data analysis.

Figures 5 and 6 show the time history of the ZPD (top panel of each figure) for days of year (DOYs) 229 and 240 from 1999. Similar plots are generated for each experiment. The top panel shows the ZPD versus time, and the bottom panel of each figure plots the site-differenced ZPD along with the best linear fit. A linear (in time) change in the zenith path delay would show up later in the analysis of the CEI data as an apparent clock drift rate. In acquiring these data, the AWVRs were pointed along the LOS and the data

Table 1. Summary of experiment dates, times, duration, and distribution during the day. (Shaded area denotes night.)

DOY	Date	Start, UT	Stop, UT	Duration, h	Universal Time, h 0	1	2	3	4	5	6	7	8	9	10	11	12	13	14	15	16	17	18	19	20	21	22	23
229	17-Aug-99	6.6	11.8									*	*	*	*	*												
240	28-Aug-99	16.3	20.3																		*	*	*	*				
263	20-Sep-99	6.5	11.2								*	*	*	*	*													
283	10-Oct-99	12.5	20.6														*	*	*	*	*	*	*	*	*			
289	16-Oct-99	19.5	24.0																					*	*	*	*	*
290		0.0	18.5		*	*	*	*	*	*	*	*	*	*	*	*	*	*	*	*	*	*						
298	25-Oct-99	2.5	13.6				*	*	*	*	*	*	*	*	*	*	*	*										
299	26-Oct-99	10	19.4												*	*	*	*	*	*	*	*	*					
300	27-Oct-99	5.3	12.2							*	*	*	*	*	*	*												
301	28-Oct-99	6.3	13.1								*	*	*	*	*	*	*											
308	4-Nov-99	4.4	10.4						*	*	*	*	*	*														
17	17-Jan-00	10.4	12.9												*	*	*											
18	18-Jan-00	11.5	14.9													*	*	*	*									
19	19-Jan-00	3.0	15.5					*	*	*	*	*	*	*	*	*	*	*	*	*								
22	22-Jan-00	4.4	14.6						*	*	*	*	*	*	*	*	*	*	*									
23	23-Jan-00	8.8	10.0												*													
24	24-Jan-00	10.5	15.6												*	*	*	*	*	*								
28	28-Jan-00	10.3	14.6												*	*	*	*	*									
34	03-Feb-00	8.2	14.2										*	*	*	*	*	*										
35	04-Feb-00	1.8	7.6				*	*	*	*	*	*	*															
39	08-Feb-00	8.6	15.8												*	*	*	*	*	*								
42	11-Feb-00	4.1	9.3							*	*	*	*															
44	13-Feb-00	7.1	9.9									*	*	*														
48	17-Feb-00	7.6	10.5										*	*	*													
94	03-Apr-00	25.4	29.8			*	*	*	*																			
105	14-Apr-00	6.3	8.0								*	*																
110	19-Apr-00	4.5	9.1						*	*	*	*	*															
116	25-Apr-00	24.4	26.8		*	*	*																					
137	16-May-00	24.3	27.1		*	*	*																					
138	17-May-00	22.8	27.1		*	*	*																					*

Table 2. Summary of surface weather conditions (from the DSS-13 weather station) during the experiments and the ZPD as estimated by the MCS at DSS 13 (A1) and DSS 15 (A2). (Columns labeled σ are the standard deviations of the individual values in the preceding column during an experiment.)

DOY	Date	Pressure, mb	σ	Temperature, deg C	σ	Relative Humidity, percent	σ	Wind Direction, deg	σ	Wind Speed, mph	σ	Average ZPD-A1, cm	σ	Average ZPD-A2, cm	σ
229	17-Aug-99	898.0	0.1	28.7	0.8	14.3	2.2	279.2	8.8	11.1	2.2	10.79	0.42	10.17	0.46
240	28-Aug-99	894.9	0.5	32.3	2.3	18.6	3.7	213.3	47.9	7.2	3.0	3.53	0.21	2.76	0.20
263	20-Sep-99	892.3	0.5	22.6	1.8	29.4	2.8	268.8	12.6	10.4	3.9	4.53	1.14	5.10	0.80
283	10-Oct-99	895.7	0.8	26.8	4.5	23.6	6.1	195.5	118.4	4.8	3.0	3.85	0.14	4.18	0.12
289	16-Oct-99	897.7	4.9	20.2	3.9	13.4	3.6	134.2	137.9	10.2	4.7	1.66	0.47	1.74	0.47
298	25-Oct-99	898.9	0.1	20.3	0.5	39.5	1.4	272.9	10.2	10.5	1.6	4.82	0.17	4.54	0.31
299	26-Oct-99	897.8	0.2	22.7	2.1	41.0	6.4	270.9	21.5	11.6	3.0	Not available			
300	27-Oct-99	895.2	0.4	20.6	0.8	39.3	1.8	264.5	13.9	18.0	3.9	5.03	0.63	5.23	0.36
301	28-Oct-99	895.1	0.6	20.5	1.1	41.4	5.8	242.9	12.2	17.8	5.0	8.50	0.89	9.16	0.96
308	4-Nov-99	Not Available										1.96	0.06	2.07	0.06
17	17-Jan-00	898.3	0.1	12.9	0.4	57.9	2.3	219.6	39.9	1.1	1.3	13.11	0.26	12.63	0.16
18	18-Jan-00	897.3	0.3	14.7	0.5	77.4	1.6	239.1	27.0	3.0	1.6	11.32	0.23	11.43	0.15
19	19-Jan-00	898.0	0.4	13.3	2.0	87.3	6.0	238.6	53.7	10.5	6.7	5.66	1.36	6.24	1.37
22	22-Jan-00	892.4	0.5	8.3	0.7	60.0	5.3	286.0	11.9	16.3	3.1	2.49	0.50	2.85	0.53
23	23-Jan-00	895.5	0.1	10.0	0.2	46.8	0.6	232.8	18.5	3.9	0.7	7.40	0.17	7.34	0.23
24	24-Jan-00	895.6	0.4	12.8	0.4	85.7	3.6	233.0	13.7	15.7	4.7	12.60	0.24	12.82	0.29
28	28-Jan-00	897.9	0.1	9.4	1.4	41.0	4.4	287.7	53.0	4.5	1.8	3.28	0.09	3.47	0.10
34	3-Feb-00	899.8	0.4	10.6	1.2	30.5	0.8	150.3	67.5	2.6	1.7	1.50	0.13	1.68	0.15
35	4-Feb-00	895.8	0.3	13.0	0.7	28.8	4.3	237.3	11.2	8.0	3.8	3.85	0.53	3.80	0.37
39	8-Feb-00	901.2	0.8	15.0	0.9	30.2	1.6	230.1	32.5	1.9	1.8	5.74	0.63	5.70	0.60
42	11-Feb-00	890.3	0.6	7.9	0.7	87.0	3.4	246.8	12.8	23.6	4.5	5.23	0.79	5.72	0.70
44	13-Feb-00	891.2	1.0	10.7	2.4	87.2	5.3	226.1	17.6	17.0	4.8	8.31	0.53	8.43	0.55
48	17-Feb-00	887.3	0.8	4.6	0.2	87.6	1.6	247.2	12.8	27.6	6.6	5.06	0.66	5.65	0.35
94	3-Apr-00	899.1	0.5	22.4	2.0	30.7	6.1	228.9	51.1	5.5	2.8	4.51	0.22	4.36	0.18
105	14-Apr-00	Not Available										4.10	0.75	4.20	0.33
110	19-Apr-00	894.2	0.3	9.9	0.1	79.0	1.6	268.4	18.6	17.4	3.9	4.73	0.42	5.56	0.17
116	25-Apr-00	893.4	0.1	28.8	1.1	13.5	0.7	233.7	21.5	7.1	1.9	2.55	0.12	3.12	0.30
137	16-May-00	887.7	0.4	14.9	1.1	45.9	3.0	254.2	13.2	26.5	6.3	4.94	0.27	5.16	0.12
138	17-May-00	890.2	0.3	25.1	0.9	28.4	1.9	185.2	111.3	6.6	3.7	6.33	0.27	5.70	0.52

Table 3. Summary of the surface meteorological data from the MCS at DSS 15 that became available starting in January 2000 and the weather instruments located at SPC 10. (σ denotes the standard deviation of the measurements during the experiment.)

		SurfMet Subsystem at DSS 15						Weather Station at SPC 10					
DOY	Date	Pressure, Mb	σ	Temperature, deg C	σ	Relative humidity, percent	σ	Pressure, Mb	σ	Temperature, deg C	σ	Relative humidity, percent	σ
17	17-Jan-00							907.6	0.1	282.7	0.2	47.5	1.8
18	18-Jan-00							906.5	0.3	283.3	0.6	70.9	1.9
19	19-Jan-00							907.5	0.4	284.2	2.2	65.0	5.8
22	22-Jan-00							902.1	0.5	279.1	1.6	49.1	5.4
23	23-Jan-00							904.8	0.1	278.7	0.3	45.3	1.5
24	24-Jan-00							905.0	0.2	283.3	0.7	67.8	4.5
28	28-Jan-00							907.7	0.5	278.0	0.9	37.7	1.2
34	03-Feb-00							909.1	0.4	279.7	1.3	31.4	1.9
35	04-Feb-00							905.0	0.4	285.5	1.4	19.4	3.4
39	08-Feb-00							910.3	0.6	283.8	0.8	24.3	0.9
42	11-Feb-00							900.2	0.6	279.6	0.8	65.5	2.6
44	13-Feb-00							900.1	0.4	279.6	0.4	66.3	2.4
48	17-Feb-00							897.4	0.6	277.0	0.2	60.4	1.7
94	03-Apr-00	908.3	0.6	295.0	3.0	18.9	3.3	908.4	0.7	295.9	2.2	16.5	3.6
105	14-Apr-00	899.6	0.1	283.6	0.4	54.6	1.1	899.8	0.2	284.2	0.8	50.2	3.3
110	19-Apr-00	904.2	0.2	278.8	1.0	75.8	4.2	904.2	0.2	279.7	1.1	67.5	4.4
116	25-Apr-00							902.7	0.1	300.4	1.2	11.0	0.0
137	16-May-00	897.7	0.3	287.5	1.2	30.8	2.8	897.8	0.3	287.2	1.0	29.9	2.7
138	17-May-00	899.5	0.3	298.1	1.3	17.1	2.2	899.8	0.5	296.0	1.0	17.9	3.1

scaled to zenith as described below. These plots offer an illustration of the dynamics of the atmosphere over 21-km baselines and are also useful for data-editing purposes.

V. Data Analysis Procedures

A. Estimating the Wet Path Delay

During the interferometry experiments, each AWVR measured the brightness temperature along its line of sight (co-pointed with the nearby DSN antenna) at 0.4-s intervals and produced a time-tagged series of data that included the AWVR azimuth and elevation angles. These brightness-temperature data were then averaged over 6-s intervals, sufficient to reduce thermal noise with no significant loss of path-delay fluctuation information. The MTP observables (13-min sampling) and SurfMet observables (1-min sampling) were then interpolated to the 6-s AWVR time tags. Thus, the complete set of time-tagged input for algorithms to estimate path delay consisted of 16 observables: 3 AWVR LOS brightness temperatures, 1 AWVR elevation angle, 9 MTP brightness temperatures (3 channels times 3 fixed elevation angles), and

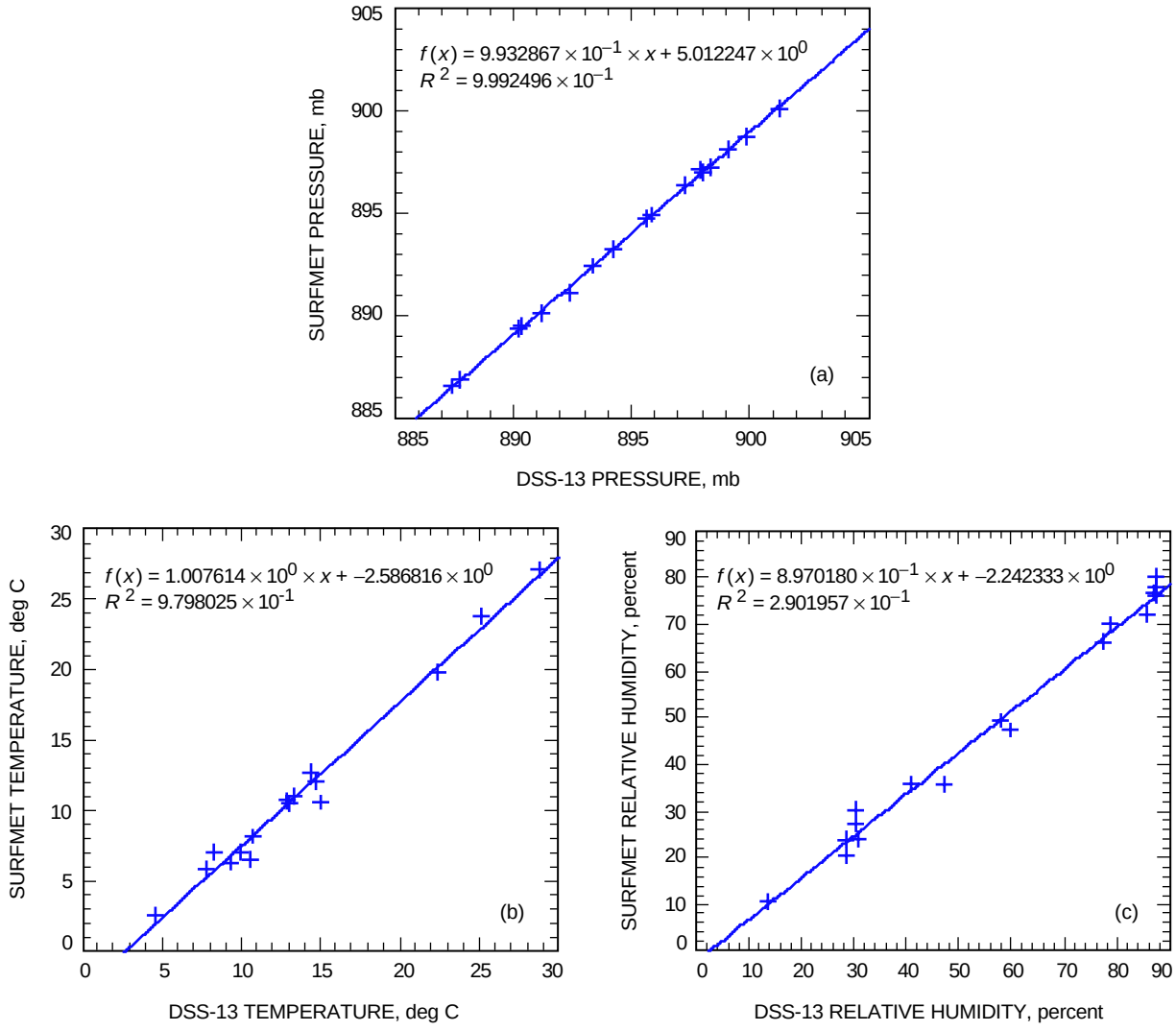

Fig. 2. Scatter plots of surface meteorological data from the DSS-13 weather station (x-axis) versus the SurfMet instruments in the MCS (y-axis): (a) pressure, (b) temperature, and (c) relative humidity. Also shown is the expression for the regression line of each plot.

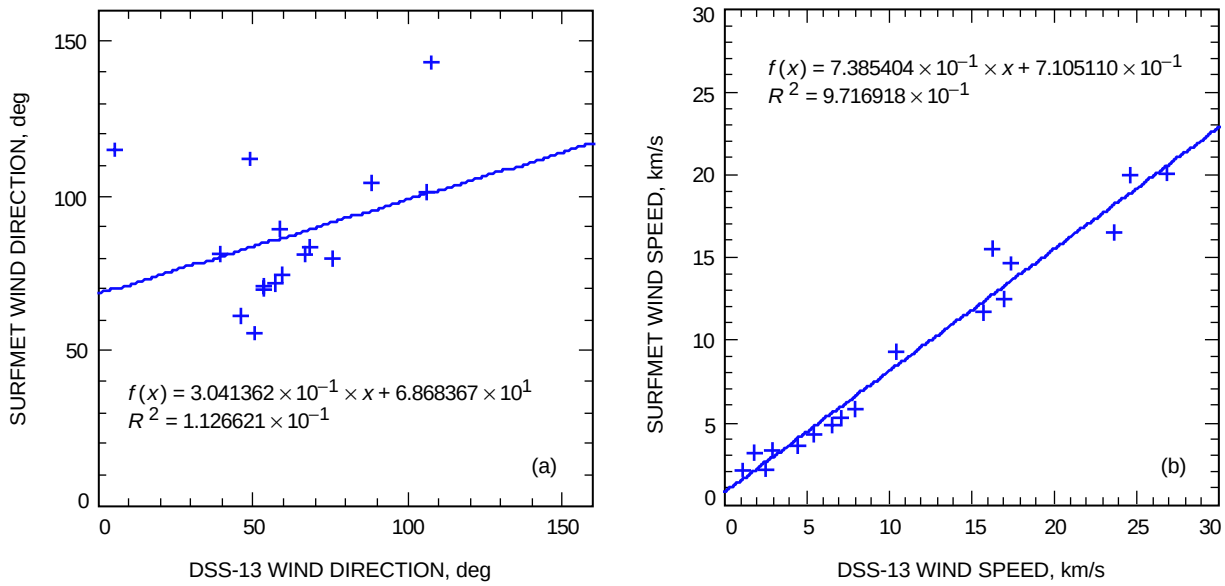

Fig. 3. Scatter plots of the (a) wind direction and (b) wind speed from the DSS-13 weather station (x-axis) and the SurfMet instruments (y-axis). Also shown are the regression line and correlation of each plot.

3 SurfMet measurements (temperature, pressure, and relative humidity). These time series were used with both a statistical retrieval algorithm [14], and, for some of the cloud-free experiments, a Bayesian retrieval algorithm [15] to estimate the line-of-sight delay.

The statistical algorithm retrieves the ZPD from a linear combination of all the observables, excepting the AWVR pointing elevation angle. The ZPD can then be converted to the elevation angle of the nearby DSN antenna (at the AWVR time tag) using an appropriate mapping function. The AWVR elevation-angle value is used first to convert the LOS brightness temperatures to zenith-equivalent values, as described below. This conversion is required to avoid the necessity of computing retrieval coefficients that depend on the time-varying AWVR elevation. By the conversion to zenith, a single set of retrieval coefficients can be applied to the entire track of an experiment. The retrieval coefficients are generated by regression fits using Desert Rock, Nevada, radiosonde-based archives of the SurfMet values, computed AWVR (zenith) and MTP (90-, 45-, and 30-deg elevation) brightness temperatures, and computed ZPD. The Desert Rock database was selected as our best match for the altitude and climatology of Goldstone. By stratifying the database according to clear-only or all-weather conditions, separate sets of retrieval coefficients were generated for clear and cloudy conditions. A simple statistical retrieval for cloud liquid burden, using only the AWVR brightness temperature measurements, $Tb(\theta)$, was implemented to determine the appropriate set of retrieval coefficients for a given experiment.

In order to implement the statistical algorithm, the brightness temperatures were first converted to zenith-equivalent values by using an approximation relating the elevation dependence of LOS brightness temperatures to zenith opacity and air mass:

$$Tb(\theta) = T_M - (T_M - T_C) \times \exp(-m \times \tau_0) \tag{1}$$

where τ_0 is the zenith opacity, $m(\theta)$ is the air mass at elevation θ, T_C is the cosmic background temperature, and T_M is the mean radiating temperature of the atmospheric emissions. One can estimate T_M from the surface-temperature measurement (using regressions from radiosonde calculations) to ∼3 K rms accuracy. Then, with the assumption of a plane-parallel atmosphere, $m(\theta) = 1/\sin(\theta)$, the zenith-equivalent brightness temperature, Tb_z, can be derived from the LOS Tb measurements as

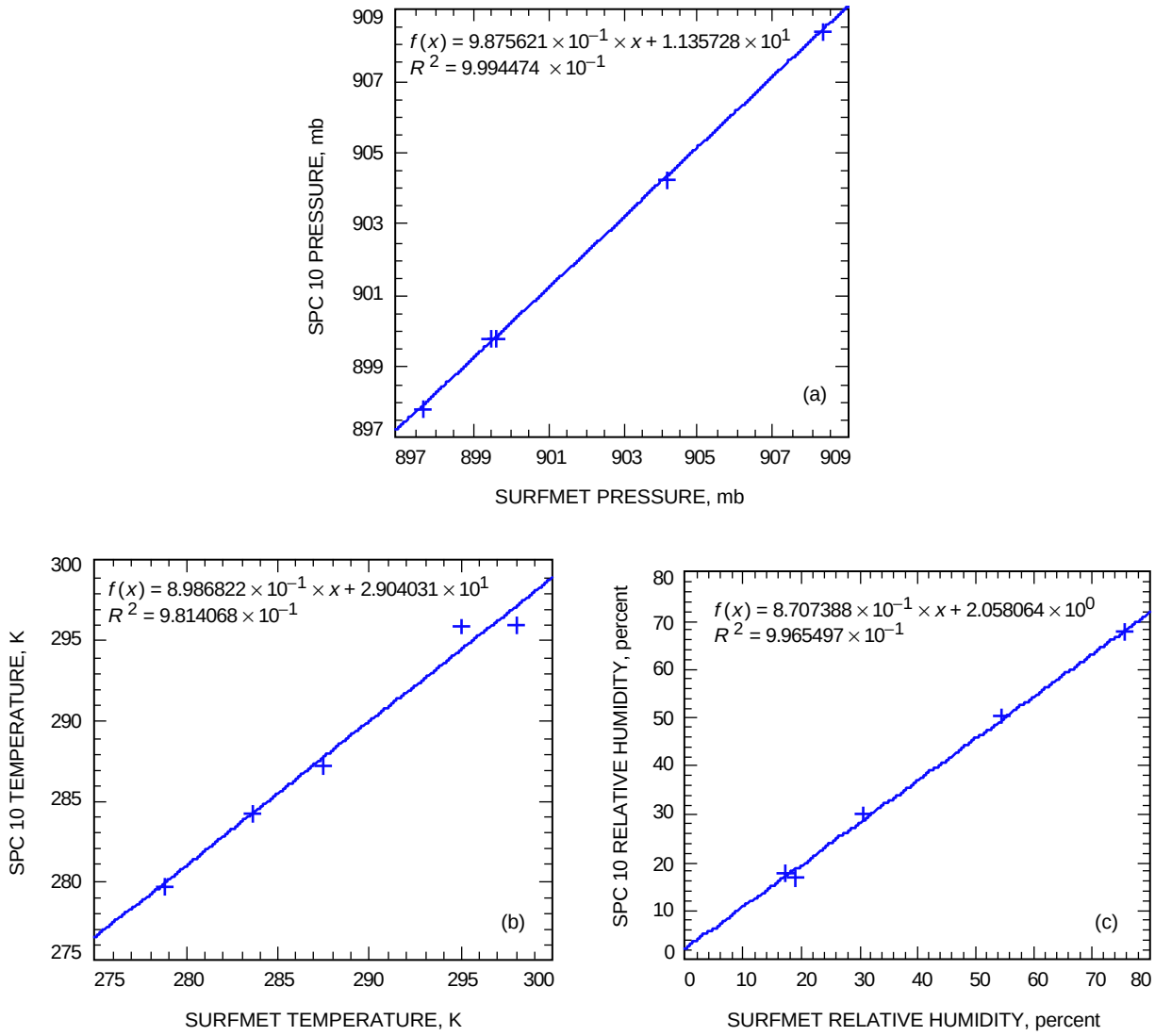

Fig. 4. Scatter plots of surface meteorological data from the SurfMet instruments located at DSS 15 (x-axis) versus the weather data from SPC 10 (y-axis): (a) pressure, (b) temperature, and (c) relative humidity. Also shown is the expression for the regression line of each plot.

$$Tb_z = Tb(\theta = 90^o) = T_M - (T_M - T_C) \times \left[\frac{T_M - Tb(\theta)}{T_M - T_C}\right]^{\sin(\theta)} \tag{2}$$

The sensitivity of the computed Tb_z in Eq. (2) to errors in T_M is small and increases with opacity. For a wet zenith delay of 10 cm, a 3-K error in T_M will cause only a 0.05-K error in the Tb_z value obtained from a 20-deg elevation LOS measurement. Simulations have confirmed that the errors in zenith delay retrieved in this way are not significantly worse than the errors in zenith delay retrieved from direct Tb_z measurements [17].

The Bayesian algorithm estimates the path delay by a direct inversion process that finds the "most probable" atmospheric state vector (surface pressure plus discrete height temperature and water-vapor density profiles) that is consistent with both the 16 measured observables and a priori statistics of the

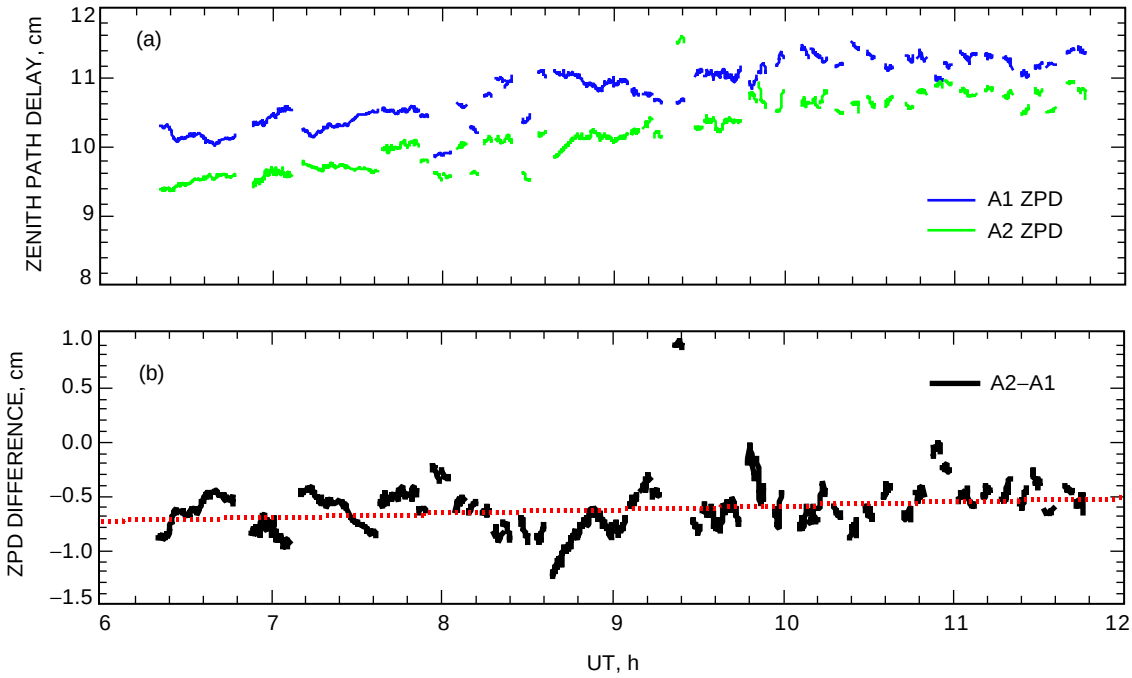

Fig. 5. The experiment on August 17, 1999 (DOY 229-1999): (a) ZPD versus time and (b) site-differenced ZPD versus time. (The AWVR denoted as A1 was located at DSS 13, and A2 was located at DSS 15.)

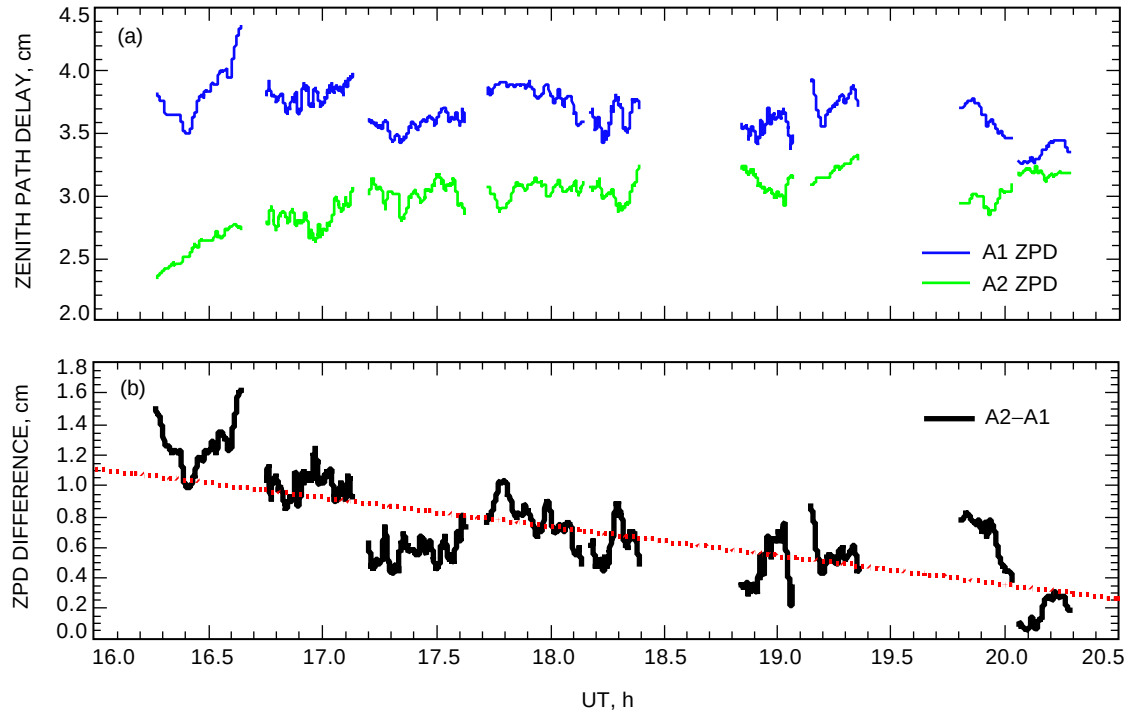

Fig. 6. The experiment on August 28, 1999 (DOY 240-1999): (a) ZPD versus time and (b) site-differenced ZPD versus time. (The AWVR denoted as A1 was located at DSS 13, and A2 was located at DSS 15.)

atmosphere (derived from the Desert Rock radiosonde archive). For a given set of observables, the candidate state vector solution "probability" depends both on its conformity to the a prior statistics and a minimization of residuals between the measured observables and theoretical observables computed from the candidate state vector using a radiative transfer model. Probabilities are computed assuming Gaussian statistics for both the components of the atmospheric state vector and the observable errors. An iterative process is implemented to find the most probable state vector, from which the zenith wet delay estimate is computed directly. For more details and comparisons of the performance of the Bayesian and statistical algorithms, see [14] and [15].

We have noted that the Bayesian algorithm is only implemented for clear conditions. Inclusion of clouds, with variable base height and thickness, and the strong temperature dependency of the absorption due to suspended water droplets lead to instabilities in the solution iteration process that make the Bayesian algorithm impractical for cloudy cases. As described in a previous study [16], the major advantages of the Bayesian algorithm are seen for clear conditions when MTP information is available. For the short-baseline interferometry experiments at Goldstone, the tropospheric temperature profiles will normally be similar enough at each end of the 21-km baseline that site-differenced path-delay retrievals will remove algorithm errors related to temperature profile effects, thereby mitigating the expected Bayesian-versus-statistical algorithm improvements expected for a single site. Thus, we have generated the more complex Bayesian algorithm solutions for only a small subset of the clear experiments and have found no significant improvement relative to the statistical algorithm.

In the development and implementation of both the statistical and Bayesian path-delay retrieval algorithms, a plane-parallel atmosphere is assumed; i.e., temperature, pressure, and humidity are assumed constant across horizontal layers. The effect of Earth curvature is to shorten the path length at the lower elevation angles, reducing both the LOS air mass and brightness temperatures by small amounts. It is straightforward to account for the curvature effect on the LOS brightness temperatures by adding a small Tb increment dependent on opacity and elevation angle.[5] However, this correction has not yet been implemented in the preliminary processing of the tropospheric calibration data for the CEI experiments. Because the final data product is the site-differenced delay over a short baseline (with nearly equal AWVR elevation angles), the small errors due to neglect of the Earth-curvature effect are expected to essentially cancel.

After the data from each set of MCS instruments were processed to produce ZPD time series at the DSS-13 and DSS-15 sites, the results were differenced to provide an estimate of the differential phase delay between the two stations that could then be compared with the CEI residual phase delay. The comparisons were made after a linear trend was removed from the site-differenced time series to provide consistency with the clock-error correction inherent to the CEI processing.

Note that the above description of media calibration processing does not include dry delay effects. For a given site, the hydrostatic (dry) zenith delay depends only on surface pressure, P_S [16]. At Goldstone, the relationship is

$$\mathrm{ZPD}_D = 0.2279 \times P_S \tag{3}$$

where P_S is the total surface pressure in millibars (mb) and ZPD is in units of cm. For the CEI experiments prior to January 15, 2000, we did not have a SurfMet station operating at DSS 15 and therefore assumed that the DSS-13 SurfMet measurements could be applied at both sites. This assumption eliminated consideration of a site-difference component due to the dry delay. Since January 15, 2000, SurfMet stations at both the DSS-13 and DSS-15 ends of the CEI baseline have been operative, and we have

[5] S. J. Keihm, "Elevation Angle and Earth Curvature Issues Relevant to the Zenith Wet Path Delay Retrieval Algorithms," JPL internal document, Jet Propulsion Laboratory, Pasadena, California, December 7, 2000.

added the small site-differenced dry delay components to the media calibration system wet delay results. Preliminary results indicate that the site-differenced dry component is rarely significant relative to the wet delay from the media calibration system in comparisons with CEI phase delay results.

The ZPD data from each MCS constitutes a time series of data, consisting of brightness-temperature fluctuations from atmospheric water-vapor and instrumental noise. After the brightness temperatures are converted to delay, we can write the time series of zenith path delay for each MCS as

$$\left.\begin{aligned} S_{W1} &= S_{atm1} + N_{W1} \\ S_{W2} &= S_{atm2} + N_{W1} \end{aligned}\right\} \tag{4}$$

These data are then differenced to provide an estimate of the differential phase delay between the two stations with the result expressed as

$$\Delta S_W = \Delta S_{atm} + N_{W1} + N_{W1} \tag{5}$$

where N_{W1} and N_{W2} are the noise contributions from the respective MCS instruments and ΔS_{atm} is the wet component of the differential atmospheric delay.

B. Interferometric Path Delay

The experiment is illustrated schematically in Fig. 1. The observable is interferometer phase delay, which is inherently a differential data type sensitive to the difference in path length between the elements of the interferometer. The difference in time of arrival, or delay τ, at the two antennas of a CEI is simply

$$\tau = \frac{\vec{B} \bullet \hat{s}}{c} + \tau_{atm} + \tau_{inst} \tag{6}$$

where $\vec{B}$ is the vector baseline between the two antennas, $\hat{s}$ is the unit vector in the direction of the source being observed, c is the speed of light, τ_{atm} is the delay due to the difference in atmospheric path, and τ_{inst} is the difference in instrumental delay.

As a radio source is tracked by the interferometer, the delay changes continuously due to Earth rotation. The cross-correlation process of the CEI data uses a priori estimates of the baseline and source position (and several other parameters as well) in order to produce residual path delay and delay rate [9]. The interferometer can be visualized as having an interference pattern in the plane of the sky with the alternate regions of in-phase and out-of-phase regions called fringes. As the radio source appears to move through these fringes, the output of the correlator is a sinusoidal variation. The correlator effectively slows this variation by modeling the changes in geometry, i.e., it calculates and subtracts the dot-product term in the equation above. In principle, we are then left with (1) the differential atmospheric delay, (2) any differences in the instrumental delay, and (3) any errors due to imperfect modeling in the correlator.

The output of the correlator is then transferred to our fringe-fitting software [17], which solves for the best estimate of the phase delay and delay rate for each scan. It also removes a term in the phase-delay estimate that is linear in time. This results in an estimate of phase delay that is zero mean over the scan and removes the constant term in the differential instrumental delay as well as any terms that are linear in time, e.g., a clock-rate offset. Next, we correct for any known error that was made in the a priori data required to run the correlator and then map the CEI data to zenith using the same mapping function as

was used with the MCS data. Note that small differences between the pointing of the AWVR and nearby 34-m antenna are reduced by this process.

The resulting time series of CEI data, which we will denote as S_I, is then approximately the difference in atmospheric delay to the two antennas plus the noise of the interferometer, or

$$S_I = \Delta S_{atm} + N_I \tag{7}$$

A graphical example of the time series represented by Eqs. (5) and (7) is shown in Fig. 7. Here we plot data from one of our first experiments, DOY 240, August 28, 1999. During this experiment, we observed nine radio sources, each for a period of 26 minutes, at a variety of elevation angles ranging from 15 deg up to 72 deg. This experiment started a little after 9 a.m. (PDT) and lasted for 3 hours. For reference, the total zenith path delays from the two MCS instruments and their difference are shown in the two panels of Fig. 6. The barometer was steady, the surface temperatures were rising at both ends of the interferometer, and the surface winds were light (i.e., 2 m/s) and from the southwesterly direction. This was a relatively dry day with moderate fluctuations at our Goldstone complex.

Figure 7 shows the residual CEI phase delay plotted on the same scale as the differenced MCS data, after a linear trend had been removed from each time series. The high degree of correlation in the fluctuations is obvious. If the interferometer and MCS instruments sense the exact same atmospheric fluctuation, ΔS_{atm}, then we can subtract the differential estimate of the LOS path delay provided by the MCS instruments from the interferometer data and we are left with

$$\begin{aligned} R_C &= S_I - \Delta S_W \\ &= N_I - (N_{W1} + N_{W2}) \end{aligned} \tag{8}$$

where $R_C = R_C(t)$ is the corrected time series. Note that the "noise" terms for both the interferometer and the AWVR contain both statistical as well as systematic error. The time series of Eq. (8) should be zero mean and have a variance of

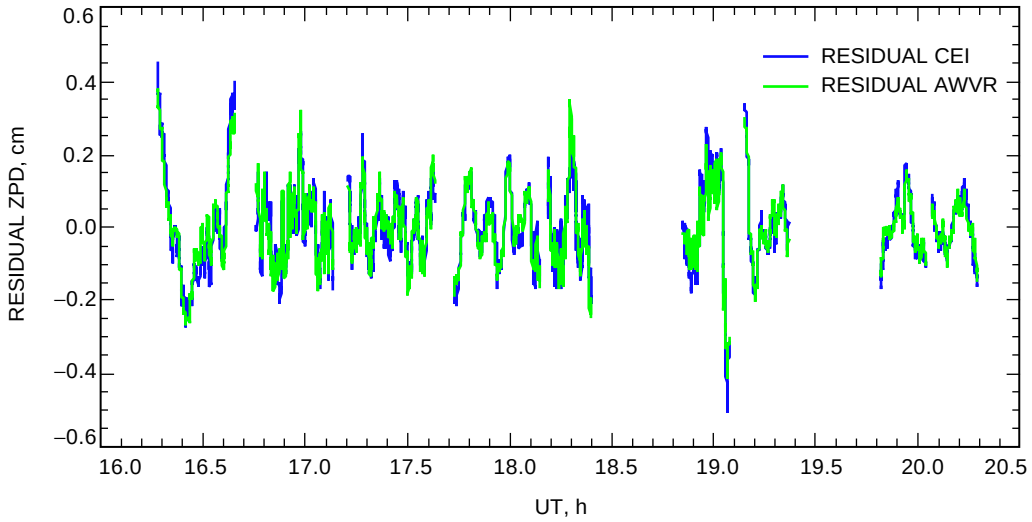

Fig. 7. The residual time delay from the interferometer and the differenced MCS data (scaled to zenith) after a linear trend is removed from each.

$$\Delta R_C^2 = \Delta N_I^2 + 2 \times \Delta N_W^2 \tag{9}$$

where we have assumed that the two MCS instruments have the same noise variance. Figure 8 shows the result of subtracting Eq. (5) from Eq. (7), i.e., calibrating the CEI residuals with the differenced MCS data. On average, the rms fluctuations are reduced by a factor of 2.7 for these 8 observations. Another way to look at these data is illustrated in Fig. 9, where we plot the histograms of the residuals for the three data types. The 2-s points of each time series for all 8 observations were binned and counted to produce these plots. We see that the broad, slightly asymmetric distributions of the CEI and MCS data, when combined, produce a much narrower and more Gaussian-looking distribution of the calibrated residuals.

Finally, we calculate the Allan standard deviation (ASD) [18] of the interferometer phase residuals before correction, using the time series given by Eq. (7), the ASD of the differenced MCS data using Eq. (5), and the corrected CEI data using the time series of Eq. (8) to assess the MCS performance. Figure 10 illustrates these ASD results for two scans taken during DOY 240, 1999, and represent the worst (scan 7) and best (scan 11) performance that day. The dotted line in each plot represents the requirement specification for the Cassini GWE.

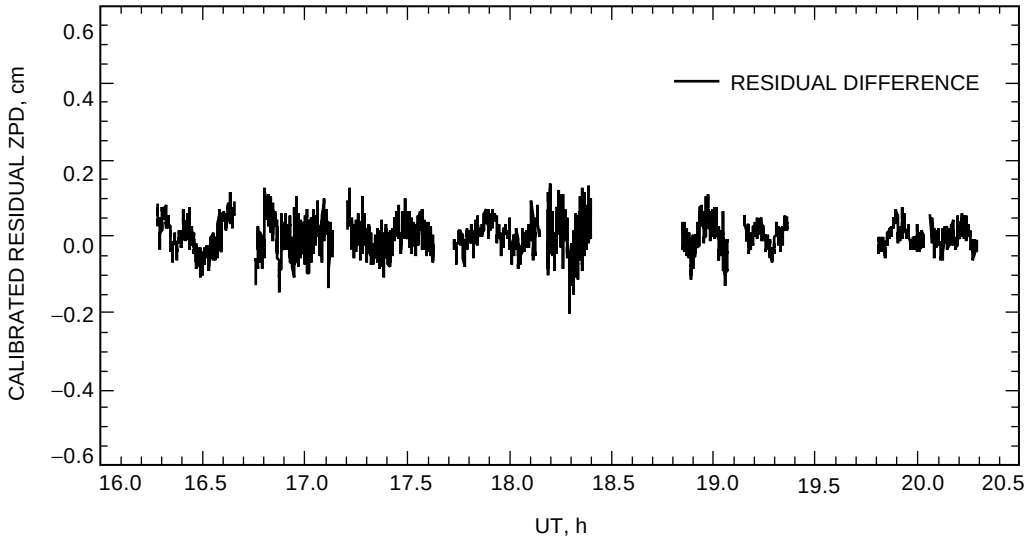

Fig. 8. The residual interferometer phase delay from after the differenced MCS was subtracted, i.e., the calibrated CEI data.

VI. Discussion

We have designed these experiments to mimic, in some respects, the Gravitational Wave Experiment that will be performed with the Cassini spacecraft during its cruise to Saturn. The GWE will involve a two-way link that will have a round-trip light-time of a few hours, whereas the experiments described here involve two receive-only antennas separated by approximately 20 km. In a sense, one can think of the experiments we describe as a spatial interferometer while the GWE is a temporal interferometer. The CEI experiments and the GWE have many common elements in their respective error budgets.

In the discussion in Section 5 regarding the comparison of the time series, we have neglected mention of systematic errors. In the case of the MCS, there are other considerations, such as the size of the AWVR sensing beam and the offset of this beam relative to that of the 34-m antenna, that will cause errors that do not appear as white noise. While we can calculate the qualitative impact of these effects [19], their actual contribution is often dependent on meteorological conditions during an experiment.

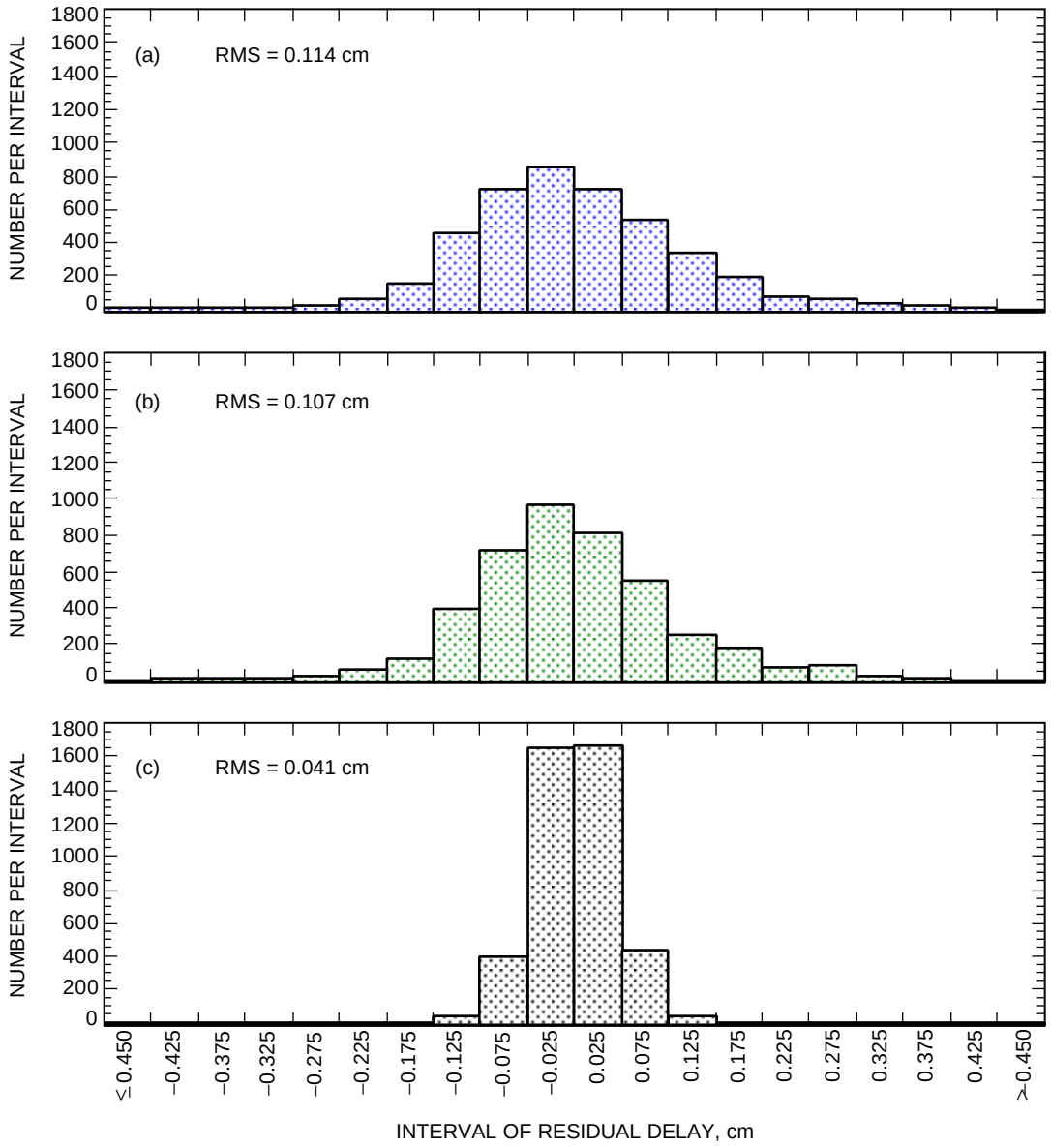

Fig. 9. Histograms of residual delays from DOY 240-1999: (a) CEI residuals, (b) AWVR residuals, and (c) calibrated CEI data.

For example, the AWVRs are located approximately 50 m from the base of the associated 34-m element of the interferometer. A "blob" of water vapor being convected horizontally at a speed of 10 km/h along the line between the AWVR and 34-m antenna will take about 18 s to make the trip. This implies we should not expect the time series discussed above to correlate very well on short time scales (e.g., <100 s), and the correlation time scale will depend on wind speed as well as where the antennas are pointing. In fact, it may depend on the wind speed at altitude rather than at the surface—a quantity we do not sense. Also, the sensing volume of the AWVR beam is approximately a cone with an opening angle of 1 deg whereas, to the 34-m antenna, the atmosphere is a near-field phenomena, and the antenna senses a

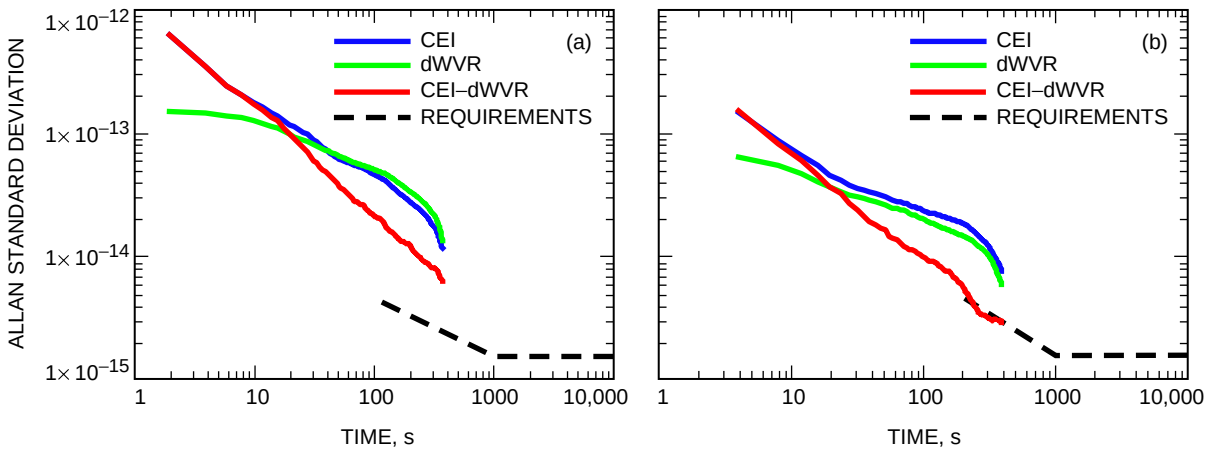

Fig. 10. ASD versus time interval from the DOY 240-1999 time series for (a) scan 7 (worst performance) and (b) scan 11 (best performance). The blue line is the ASD of the CEI residuals, green is the differenced AWVR residuals (dWVR), and red is the CEI data that were calibrated with the dWVR data. The dotted line shows the requirements for the Cassini Gravitational Wave Experiment.

cylindrical volume. Again, this difference would lead us to not expect short-term correlation in the data. Indeed we have found that short-term correlation, when present, is highly variable.[6]

The error budget for the CEI is even more complex than that for the AWVR. The typical precision of a high SNR CEI measurement is sub-picosecond (ps), where 1 ps corresponds to a distance of 0.3 mm. The ultimate accuracy of the measurement is limited by systematic effects that enter on a variety of time scales. We wish to isolate the atmospheric term in Eq. (6), so we model the changing geometry (i.e., the $\vec{B} \bullet \hat{s}$ term) and remove a constant bias plus a term linear in time, i.e., a clock-rate term, from the resulting phase delay. Many of the errors that are possible either in the modeling or in the instrumental delay term, τ_{inst}, appear to be constant or slowly varying for short periods of time and, therefore, are removed by this process.

Geometrically related CEI errors have diurnal signatures that appear linear in time for short observations but quadratic (or higher order) for longer observations. For example, we know that errors occur in the correlator model due to insufficient a priori information, and we attempt to reduce them by making corrections in the post-fit analysis. Examples are (1) small differences due to the dry component of the troposphere, (2) small changes in baseline orientation due to variable Earth rotation (i.e., UT1–UTC corrections and polar motion), and (3) improved knowledge of the baseline components. On average, for long scans, the geometrically related corrections improved the residuals by ∼8 percent. The dry delay error correction, which includes both a static correction to the correlator model and variations in the dry delay error due to mapping errors and surface conditions, improved residuals from 0 to 5 percent, depending upon the weather conditions.

There are other CEI errors that are much more difficult to model at the picosecond level. Examples include antenna deformation due to gravity and wind, thermal effects in the electronics and antenna structure, frequency distribution system, etc. To the extent that these errors are not common mode at the two ends of the interferometer, they will appear as systematic effects in our data. Most of these errors will also be present during the GWE.

[6] The complete error budget for the media calibration system is discussed in R. P. Linfield, "Error Budget for WVR-Based Tropospheric Calibration System," JPL Interoffice Memorandum 35.1-96-012 (internal document), Jet Propulsion Laboratory, Pasadena, California, June 5, 1996.

VII. Summary

The data described in this article are currently being analyzed. Preliminary analysis suggests the new media calibration system does meet Cassini requirements some of the time. At this juncture, the limiting factor in the comparison between CEI and the MCS is not clear, but we strongly suspect systematic errors in the CEI data.

In late 2000 there was a significant upgrade to the frequency distribution system between SPC 10 and DSS 13 that we expect will improve CEI long-term performance, and additional experiments were conducted between December 2000 and February 2001. These experiments and results of the analysis of experiments described here will be described in a future issue of this publication.

Acknowledgments

We are very grateful to Lyle Skjerve, Leroy Tanida, Charles Snedeker, the staff at DSS 13, and the Operations crews at the Goldstone Signal Processing Center for the invaluable assistance they provided during these experiments.

References

[1] J. W. Armstrong, B. Bertotti, F. B. Estabrook, L. Iess, and H. D. Wahlquist, "The Galileo/Mars Observer/Ulysses Coincidence Experiment," *Proc. of the Second Edoardo Amaldi Conf. on Gravitational Waves*, edited by E. Coccia, G. Pizzella, and G. Veneziano, Edoardo Amaldi Foundation Series, vol. 4, World Scientific, Geneva, Switzerland, July 1–4, 1997, pp. 159–167, 1998.

[2] M. Tinto and J. W. Armstrong "Spacecraft Doppler Tracking as a Narrow-Band Detector of Gravitational Radiation," *Phys. Rev. D*, vol. 58, 042002, pp. 042002-1–042002-8, 1998.

[3] G. M. Resch, C. Jacobs, S. Keihm, G. Lanyi, C. Naudet, A. Riley, H. Rosenberger, and A. Tanner, "Calibration of Atmospherically Induced Delay Fluctuations due to Water Vapor," *International VLBI Service for Geodesy and Astrometry 2000 General Meeting Proceedings*, edited by N. R. Vandenberg and K. D. Baver, NASA/CP-2000-209893, Kötzting, Germany, pp. 274–279, 2000.

[4] C. Naudet, C. Jacobs, S. Keihm, G. Lanyi, R. Linfield, G. Resch, L. Riley, H. Rosenberger, and A. Tanner, "The Media Calibration System for Cassini Radio Science: Part I," *The Telecommunications and Mission Operations Progress Report 42-143, July–September 2000*, Jet Propulsion Laboratory, Pasadena, California, pp. 1–8, November 15, 2000.
http://tmo.jpl.nasa.gov/tmo/progress_report/42-143/143I.pdf

[5] G. M. Resch, D. E. Hogg, and P. J. Napier, "Radiometric Correction of Atmospheric Path Length Fluctuations in Interferometric Experiments," *Radio Sci.*, vol. 19, pp. 411–422, January 1984.

[6] L. P. Teitelbaum, S. J. Keihm, R. P. Linfield, M. J. Mahoney, and G. M. Resch, "A Demonstration of Precise Calibration of Tropospheric Delay Fluctuations with Water Vapor Radiometers," *Geophys. Res. Lett.*, vol. 23, no. 25, pp. 3719–3722, December 1996.

[7] C. Edwards, Jr., D. Rogstad, D. Fort, L. White, and B. Iijima, "The Goldstone Real-Time Connected Element Interferometer," *The Telecommunications and Data Acquisition Progress Report 42-110, April–June 1992*, Jet Propulsion Laboratory, Pasadena, California, pp. 52–62, August 15, 1992.
http://tmo.jpl.nasa.gov/tmo/progress_report/42-110/110D.PDF

[8] G. Lutes and A. Kirk, "Reference Frequency Transmission Over Optical Fiber," *The Telecommunications and Data Acquisition Progress Report 42-87, July–September 1986*, Jet Propulsion Laboratory, Pasadena, California, pp. 1–9, November 15, 1986.
http://tmo.jpl.nasa.gov/tmo/progress_report/42-87/87A.PDF

[9] J. B. Thomas, *Interferometric Theory for the Block II Processor*, JPL Publication 87-29, Jet Propulsion Laboratory, Pasadena, California, October 15, 1987.

[10] A. B. Tanner, "Development of a High-Stability Water Vapor Radiometer," *Radio Sci.*, vol. 33, pp. 449–462, March 1998.

[11] *TP-2500 Temperature Profiling Radiometer*, User's Manual, Radiometrics Corporation, Boulder, Colorado, November 1998.

[12] *Met3 Meteorological Measurement System*, Document T8360-001, Rev. D, Paroscientific, Inc., Redmond, Washington, 1999.

[13] *Sonic Anenometer, Manual for p/n M102263*, Climatronics Corp., Bohemia, New York, 1999.

[14] G. M. Resch, M. C. Chavez, N. I. Yamane, K. M. Barbier, and R. C. Chandlee, *Water Vapor Radiometry Research and Development Phase Final Report*, JPL Publication 85-14, Jet Propulsion Laboratory, Pasadena, California, April 1, 1985.

[15] S. J. Keihm and S. Marsh, "New Model-Based Bayesian Inversion Algorithm for the Retrieval of Wet Tropospheric Path Delay from Radiometric Measurements," *Radio Sci.*, vol. 33, no. 2, pp. 411–419, March 1998.

[16] J. Saastamoinnen, "Atmospheric Correction for the Troposphere and Stratosphere in Radio Ranging of Satellites," in *The Use of Artificial Satellites for Geodesy*, Geophysics Monograph, series 15, American Geophysical Union, pp. 247–251, 1972.

[17] S. Lowe, *Theory of Post-Block II VLBI Observable Extraction*, JPL Publication 92-7, Jet Propulsion Laboratory, Pasadena, California, July 15, 1992.

[18] D. W. Allan, "Statistics of Atomic Frequency Standards," *Proc. IEEE*, vol. 54, no. 2, pp. 221–230, February 1966.

[19] R. P. Linfield and J. Z. Wilcox, "Radio Metric Errors Due to Mismatch and Offset Between a DSN Antenna Beam and the Beam of a Tropospheric Calibration Instrument," *The Telecommunications and Data Acquisition Progress Report 42-114, April–June 1993*, Jet Propulsion Laboratory, Pasadena, California, pp. 1–13, August 15, 1993.
http://tmo.jpl.nasa.gov/tmo/progress_report/42-114/114A.pdf